Author/s:
Fernandes, G;Di Prima, S;Lipeme Kouyi, G;Fletcher, TD;Donze, D;James, R;Saint-Louis, SM;Martini, M;Nicklason, C;Lassabatere, L

Title:
A novel method to assess the infiltration and filtration functions of urban soils

Date:
2025-11-01

Citation:
Fernandes, G., Di Prima, S., Lipeme Kouyi, G., Fletcher, T. D., Donze, D., James, R., Saint-Louis, S. M., Martini, M., Nicklason, C. & Lassabatere, L. (2025). A novel method to assess the infiltration and filtration functions of urban soils. Vadose Zone Journal, 24 (6), https://doi.org/10.1002/vzj2.70050.

Persistent Link:
https://hdl.handle.net/11343/369550

Received: 17 March 2025 | Accepted: 21 September 2025

DOI: 10.1002/vzj2.70050

Vadose Zone Journal

ORIGINAL ARTICLE

A novel method to assess the infiltration and filtration functions of urban soils

Gersende Fernandes[1,2] | **Simone Di Prima**[3] | **Gislain Lipeme Kouyi**[2] | **Tim D. Fletcher**[4] | **Daniel Donze**[1] | **Robert James**[4] | **Saint-Martin Saint-Louis**[1] | **Matteo Martini**[5] | **Claudia Nicklason**[4] | **Laurent Lassabatere**[1]

[1]Université Claude Bernard, Lyon 1, LEHNA UMR 5023, CNRS, ENTPE, Vaulx-en-Velin F-69518, France

[2]INSA Lyon, DEEP, UR7429, Villeurbanne 69621, France

[3]Department of Agricultural, Forestry, Food and Environmental Sciences (DAFE), University of Basilicata, Potenza 85100, Italy

[4]School of Agriculture, Food and Ecosystem Sciences (SAFES), University of Melbourne, Victoria 3010, Australia

[5]Institute of Light and Matter, UMR 5306, University of Lyon 1-CNRS, University of Lyon 1, Villeurbanne Cedex, France

Correspondence
Gersende Fernandes, Université Claude Bernard Lyon 1, LEHNA UMR 5023, CNRS, ENTPE, Vaulx-en-Velin F-69518, France.
Email: gersende.fernandes@inrae.fr

Assigned to Associate Editor Chao Zhou.

Funding information
Australian Research Council, Grant/Award Number: ARC IL230100020; Agence Nationale de la Recherche, Grant/Award Numbers: ANR-17- EURE-0018, ANR-17-CE04-010

Abstract

Urban areas are increasingly under pressure due to rapid expansion and extreme rainfall events driven by climate change. Rather than relying solely on pipes to regulate stormwater, new management systems promote direct infiltration of water and pollutants into the soil. Soils fulfill multiple functions, including water infiltration and pollutant filtration. Urban soils, however, are often highly heterogeneous; the presence of macropores can accelerate water flow while reducing pollutant retention. Yet, infiltration and filtration are typically assessed using surface measurements and soil-destructive methods, which fail to capture the complexity of water and pollutant transport pathways in the subsurface. In this study, we present a prototype of a large-ring infiltrometer coupled with a ground-penetrating radar (GPR) to simultaneously monitor water and nanotracers movement in the subsurface. This provides a more comprehensive characterization of both infiltration and filtration functions. Superparamagnetic iron oxide nanoparticles (SPIONs) were chosen as nanotracers due to their nontoxicity, small size, and advantageous electromagnetic properties. Although distinguishing between subsurface zones imbibed with water and those containing SPIONs was challenging, GPR imaging revealed distinct spatial patterns and temporal dynamics even under identical infiltration conditions. Comparative analyses with water and solute transport models further elucidated the underlying subsurface processes. Typologies of infiltration and filtration patterns, linked to soil heterogeneity, are presented. Our results emphasize the need for a more comprehensive characterization of infiltration and filtration functions to improve flood risk assessment and evaluations of groundwater pollution threats.

Abbreviations: GPR, ground-penetrating radar; SLA, Survey Line A; SLB, Survey Line B; SPION, superparamagnetic iron oxide nanoparticle.

Plain Language Summary

In cities, soil imperviousness increases runoff and pollutant concentrations in stormwater. New stormwater management systems allow water to infiltrate into the soil, retaining pollutants and restoring a more natural water cycle. To monitor the risk of groundwater contamination, we developed INFILTRON-Exp, an experimental setup for the simultaneous characterization of soil's water infiltration and pollutant filtration. This setup addresses the limitations of traditional infiltration measures, which focus only on surface processes. We used ground-penetrating radar, which can probe below the surface to (i) improve infiltration analysis by identifying different types of subsurface water flows and (ii) study filtration by tracking magnetic nanoparticles that mimic pollutants. Finally, we combined experimental data with flow and transport modeling to validate the observed subsurface patterns.

1 | INTRODUCTION

In urban soils, the water cycle is profoundly changed compared with other pervious areas (such as agricultural land or forests): infiltration decreases and runoff increases, leading to increased flows of (typically contaminated) stormwater (Grimm et al., 2008). To reverse this trend, new approaches to stormwater management are being developed in cities, based in part on the direct infiltration of stormwater into soils (Hatt et al., 2009). However, urban stormwater contains a variety of pollutants, including metallic trace elements (e.g., lead, copper, and zinc), persistent emerging pollutants such as polycyclic aromatic hydrocarbons (PAHs), polychlorinated biphenyls, bacteria, and nanoparticles, many of which pose risks to both the environment and human health (Aryal et al., 2010; Pinasseau et al., 2020). In particular, sustainable urban drainage systems accumulate some pollutants at their surface (Tedoldi et al., 2016). In recent years, increasing attention has been directed toward nanometric pollutants, whose presence and potential ecological and public health hazards are well-documented (Ghangrekar & Chatterjee, 2018). These pollutants primarily originate from runoff on impervious surfaces that accumulate harmful substances, such as waste materials, automobile residues, and agrochemical products (Müller et al., 2020). As runoff flows through urban drainage systems, pollutants are transported with infiltration into the soil. It offers an opportunity for their retention, thereby preventing contamination of receiving environments—particularly groundwater.

Restoring the natural water cycle in urban areas requires promoting water infiltration while ensuring that pollutants are retained in the upper soil layers to protect groundwater quality. In this context, the ecosystem functions of urban soils offer a valuable opportunity. Infiltration and filtration are two of the numerous functions provided by soils, which also include habitat provision, element cycling, decomposition, biological population regulation, organic matter cycling, and water cycling (Bünemann et al., 2018). The determination and quantification of the soil functions allow the characterization of soil ecosystem services, and thus the assessment of soil quality or soil health. This study focuses on improving two aspects of the water cycle's function in soils that influence both quantity and quality assessments: the infiltration and filtration functions.

Infiltration is the physical process by which water enters the soil surface and therefore depends on the soil's texture and structure. Soils are heterogeneous and made up of complex media, which complicates the prediction of the movement of solids, liquids, and gases. Urban soils, in particular, are highly heterogeneous due to various external material inputs and the mixing of the initial soil material. Preferential flows can arise from various forms of soil heterogeneity, such as significant lithological heterogeneity at a large scale or soil systems with different porosity and permeability at the point scale. At this scale, it is well known that soil texture and structure influence the number and size of pores participating in flow, which in turn affects water infiltration (Angulo-Jaramillo et al., 2016). In macropores, the velocity of water is higher than in smaller pores, the latter being also known as the soil matrix (Köhne et al., 2009). In the field, several devices and related protocols to measure infiltration are available (Angulo-Jaramillo et al., 2000). These devices allow for the determination of cumulative infiltration and infiltration rate over time, enabling the quantification of the infiltration function. However, they do not provide direct information on soil heterogeneity or on the complexity of flow patterns, both of which are critical for understanding pollutant transport.

The soil's filtration function—its ability to retain and immobilize pollutants—depends on the physicochemical properties of the soil, the nature of the pollutants, and their interactions with soil particles in the presence of water (Chéry & Mouvet, 2000). Citeau (2008) highlights that pollutants such as trace metals and apolar organic compounds (e.g., PAHs, phthalates) are retained in the upper soil layers through size-dependent mechanisms: larger particles are captured by settling, while smaller ones are filtered (Sage, 2018). However, preferential flow paths within the soil can significantly reduce the filtration function by increasing water flow velocity and decreasing pollutant interaction with reactive soil particles (Lassabatere et al., 2004), diminishing the soil's capacity for filtration and increasing risks to groundwater (Köhne et al., 2009). In addition to pollutants carried by stormwater, urban soils and sustainable urban drainage systems accumulate pollutants at the surface (Tedoldi et al., 2016), which can potentially be released. Numerous tools are available to investigate pollution concentrations, transport, and fate in various environmental contexts (Singh et al., 2018). Laboratory experiments, for example, often conducted using soil-filled columns, provide a controlled environment for investigating the transport of colloids and pollutants (Mori & Hirai, 2014; Wang et al., 2020). However, these laboratory experiments must be combined with field experiments under real conditions.

In field studies, experiments are often destructive and lack precise spatial information. Common methodologies include soil dye-staining with agents such as uranine, brilliant blue for coloring food (FCF), or methylene blue during rainfall or infiltration experiments (Alaoui et al., 2011; Allaire et al., 2009; Kodešová et al., 2012). Dye can also be sprinkled during experiments (Gerke et al., 2015). Alternatively, tracers such as ^{18}O-enriched water, salts, or bromide are used to track water and solute movement (Allaire et al., 2009; Angulo-Jaramillo et al., 2000). However, these techniques require soil excavation, which is labor-intensive, time-consuming, and environmentally disruptive. Additionally, such approaches provide only discrete, noncontinuous information, leading to gaps in spatial data and environmental impacts. Most of the methods used for studying pollutant retention and release provide quantitative data without precise spatial resolution (Núñez-Delgado, 2024). Lastly, pollutants cannot be injected on the field due to their toxicity, inducing a gap of knowledge about their transfer behavior in real environments. While pollutant concentration variations can be measured, their exact locations within the soil remain difficult to determine.

This study presents INFILTRON-Exp, a novel experimental setup that combines large-ring infiltrometer tests with ground-penetrating radar (GPR), specifically designed for the simultaneous characterization of infiltration and filtration functions. Indeed, the setup enables the detection of flow pathways and the transport of specific nanotracers engineered to mimic the contrasting behaviors of pollutants. Superparamagnetic iron oxide nanoparticles (SPIONs) coated with silica were chosen as model nanopollutants due to their (i) nontoxicity (Li et al., 2013), (ii) potential detectability with the GPR, owing to their distinct dielectric and magnetic properties, and (iii) surface functionalization capabilities, allowing for the simulation of various nanopollutant behaviors during infiltration. Functionalization enables SPIONs to mimic different pollutant behaviors based on positive or negative surface charges. To date, no other nanotracers with these characteristics have been identified. While this approach does not fully represent the heterogeneity of pollutants present in urban runoff, it serves as a first step toward improving subsurface pollutant tracking and mimicking contrasted behaviors for pollutants. To the best of our knowledge, no studies have combined SPIONs with GPR to simulate pollutant behavior in soils. The primary objective of this research is to identify infiltration and filtration patterns, and relate them to the processes governing water flow and pollutant transport. This will support the development of more comprehensive and qualitative representations of infiltration and filtration functions.

Core Ideas

- We developed INFILTRON-Exp, an original experimental setup for the simultaneous assessment of the infiltration and filtration functions.
- Cumulative infiltration and infiltration rates are insufficient to fully describe the infiltration function.
- Typologies of water flows at the subsurface, determined with GPR, improve the understanding of the infiltration function.
- Superparamagnetic iron oxide nanoparticles were used to simulate pollutant behavior during the infiltration experiment.
- GPR visualization, combined with flow and transport modeling, provides valuable insights into both infiltration and filtration functions.

2 | MATERIAL AND METHODS

2.1 | INFILTRON-Exp package (infiltrometer and GPR)

INFILTRON-Exp technology is a package developed by the authors, consisting of (i) a large infiltrometer and (ii) a GPR. The large size of the infiltrometer increases the likelihood of capturing different sources of soil heterogeneity (e.g., cracks, macropores, fractional wettability), thereby providing a more representative characterization of soil heterogeneity.

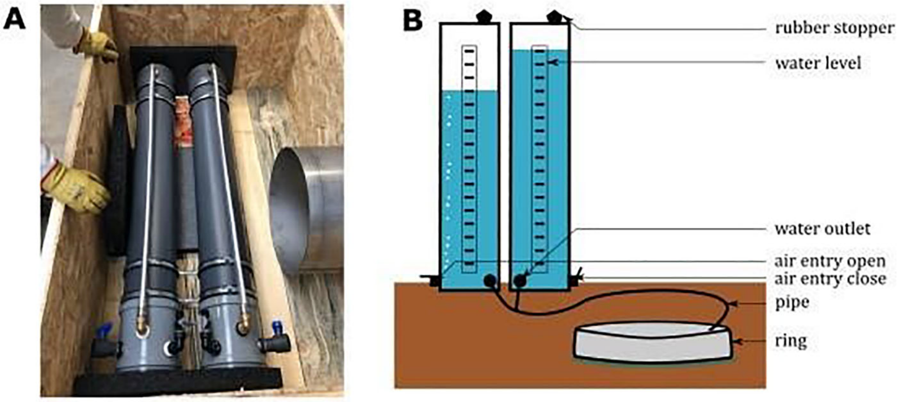

FIGURE 1 Large infiltrometer (A) photo and (B) scheme with the different constitutive parts.

This device is specifically designed to simultaneously and in real time assess both infiltration and filtration functions by tracking water flow and nanotracers in the field. Its uniqueness lies in the combination of an infiltrometer and GPR, which enables visualization of water flow and potential detection of nanotracers. While GPR has previously been used to monitor water movement, to our knowledge, it has never been applied to precisely detect nanotracers.

The large infiltrometer combines a stainless-steel ring with an inner diameter of 50 cm and two columns serving as reservoirs (Figure 1). The cylindrical columns are made of polyvinyl chloride (PVC), each with a height of 110 cm and a diameter of 20 cm. They are equipped with an external transparent level tube, connected at both ends, to monitor the decrease in water levels inside. At the lower parts of the columns, there is a water supply valve and an air-entry valve positioned above. The water supply valve is a ball valve located 5 cm above the bottom of the column, allowing for the attachment of plastic pipes. Each column can be filled from the top and then sealed with a rubber plug. The total volume of water stored in the two columns (~70 L) results in a total infiltration amount of approximately 350 mm, which is the same as that of the automated infiltrometers developed by Concialdi et al. (2020) and Di Prima et al. (2015), with a 15 cm-diameter ring. The 50 cm-diameter ring in INFILTRON-Exp is designed to sample a large enough soil area to optimize the likelihood of intercepting macropore networks and activating all types of pores in the soil. Larger double-ring infiltrometers have been proved efficient to decrease hydraulic conductivity variability and for reliable measurement (Lai & Ren, 2007). This 50 cm diameter is significantly larger than the standard rings used for single-ring infiltrometers. The reservoirs and the ring are connected by a three-way connector pipe, with two ends that connect to the reservoirs and a third end with a metallic header valve that can be positioned in the ring. The principle of INFILTRON-Exp aligns with the functioning of a single-ring infiltrometer (Angulo-Jaramillo et al., 2000). It follows the Beerkan method (Lassabatère et al., 2006), initially developed for manual single-ring experiments and later adapted to automated infiltrometers by Di Prima (2015).

2.2 | Assessment of the infiltration and the filtration functions

The soil's hydraulic characterization is usually performed by plotting the cumulative infiltration curves and the final infiltration rate curves, which serve as direct indicators of the infiltration function. The experimental data used for both infiltration and filtration functions are presented in Figure 2. The volume of water infiltrated can be calculated directly from the water level drop in the reservoir, using the mass balance equation, leading to the following expression for the cumulative infiltration $I(t)$:

$$I\ (t) = \frac{R^2}{r_\mathrm{d}^2}\ H\ (t) \tag{1}$$

where $H(t)$ corresponds to the height of water in the reservoir at time t, R is the radius of the reservoir, and r_d is the radius of the ring. The R software R Core Team (2024) is used for the plotting. The infiltration function will then be assessed on the basis of the cumulative infiltration. Further developments, such as the estimation of the soil's hydraulic properties, could be proposed; however, this aspect was not considered for the sake of simplicity. Instead, in addition to assessing the soil's bulk infiltration capacity, we focused on detecting flow pathways using GPR.

To assess the filtration function, we monitored the movement of nanotracers by detecting their presence in the soil and tracking their spatial distribution over time (Figure 2). Unlike lysimeters, which measure flux at a specific depth, our approach relied exclusively on a nonintrusive technique: the detection of nanotracers and the estimation of their concentration (or at least their presence) within the soil. The processing of GPR signals used to determine the pathways of water and nanotracers is described in the following sections.

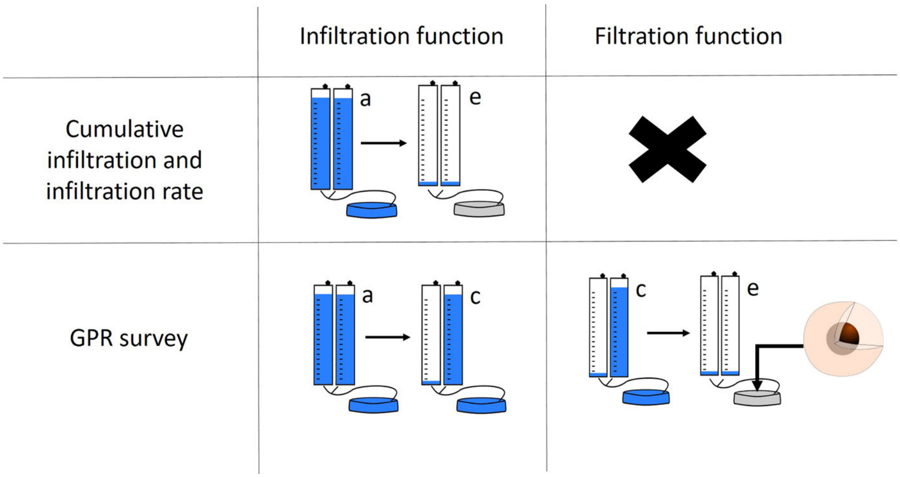

FIGURE 2 Summary of the data and infiltration stages (“a”, “c”, and “e”) used to calculate infiltration parameters (cumulative infiltration and infiltration rate) and generate ground-penetrating radar (GPR) visualizations. Stage “a” corresponds to the beginning of the infiltration test, stage “c” to the middle, and stage “e” to the end (see Figure 3 for details).

TABLE 1 Experimental information for the three sites (IUT, ENTPE [Engineering School of Sustainable Land Planning], Burnley): total tests conducted, tests using ground-penetrating radar (GPR), and their names.

Parameters	ENTPE	IUT	Burnley
Infiltration experiments (total)	9	15	2
Infiltration experiment with GPR	1 (no nanotracer injected)	5	2
GPR tests names	Test 1 (Strategy 1)	Tests 2–6 (Strategy 1)	Tests 7 and 8 (Strategy 2)

2.3 | Experimental site and field measures

INFILTRON-Exp was tested on three different sites: “ENTPE” (Engineering School of Sustainable Land Planning) and “IUT” in France, and “Burnley” in Australia. A first series of infiltration experiment was performed in France to validate the accuracy of the infiltration and the continuity of the water infiltration rate between the two reservoirs of the infiltrometer (see below) in summer 2019. The following series was then carried out, adding GPR acquisition to the infiltration experiments, from July to October 2022 in France and in April 2023 in Australia. Table 1 summarizes all the tests done by the site. At the ENTPE site, nine tests were conducted using the infiltrometer including one with GPR (named Test 1). At the IUT site, 15 tests were conducted, including five with GPR (Tests 2–6). At the Burnley site, two tests with GPR were conducted (Tests 7 and 8). Two different types of grid installations and sampling strategies with GPR were used in France and then in Australia (Strategy 1 and Strategy 2; see Figure 3 and below).

The first French site was located on the campus of the ENTPE in Vaulx-en-Velin. The sampled area was also composed of grass and trees over the same glaciofluvial deposit that covers most of the region of Lyon. The soil texture is loamy sand.

The second site was located on the campus of La Doua (Villeurbanne, France) and is close to the so-called IUT infiltration basin. The infiltration basin infiltrates stormwater collected from part of the campus into a few-meter-depth vadose zone. Inside the basins, rocks and pebbles at the soil surface prevented us from installing the infiltrometer ring. Consequently, the tests were performed on the banks of the infiltration basin. The sampled area was grassed, with the first upper horizon constituted of vegetative soil above a glaciofluvial deposit. The soil texture is loamy sand.

In Australia, the site was located on the Burnley campus of the University of Melbourne. The sampled area was a newly built subsurface porous media drain beneath 50 cm of sand, with the surface covered by grass.

For all sites except Burnley, the proximity of trees suggests a significant possible presence of preferential flows associated with the presence of roots (Di Prima et al., 2021, 2023).

2.4 | Deployment of INFILTRON-Exp on the field

The installation begins by preparing the surface: delineating a flat area and mowing the grass to ground level while preserving the roots and macropores beneath the soil surface.

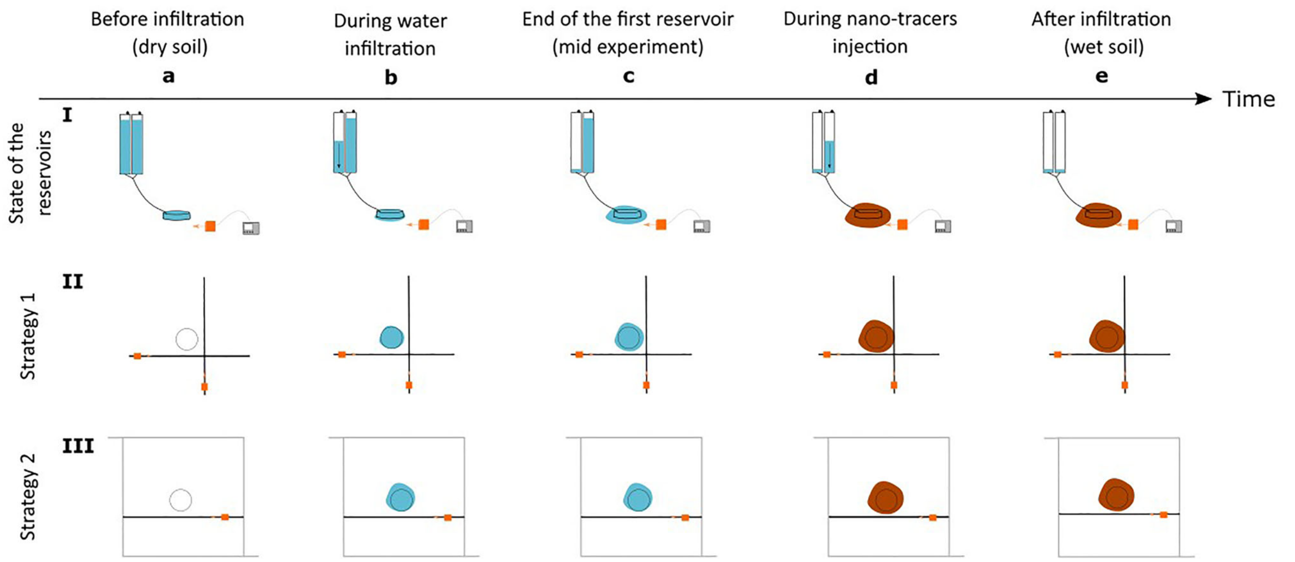

FIGURE 3 Steps of water and nanotracer injection experiments in time, illustrated from (a) to (e). Ground-penetrating radar (GPR) surveys were conducted using (II) Strategy 1 in France and (III) Strategy 2 in Australia. Additional details on the state of the reservoirs are provided in Section 1. The orange square represents the GPR, and the black lines represent the surveyed lines.

The ring is then inserted 5 cm into the ground. The two water-filled column reservoirs are positioned 1 m away from the ring, with the water in each reservoir reaching a height of 115 cm.

To adjust the water pressure within the columns, the latter are sealed, and the air-entry valves are opened. A specific volume of water is then poured onto a plastic sheet placed inside the ring. The two reservoirs are connected to the ring using a Y-system pipe, ensuring no air bubbles are introduced. The water-supply valve of the first reservoir is opened, and the water level inside the ring is adjusted to achieve equilibrium. For most experiments, the average water depth within the ring is maintained between 8 and 10 cm. The GPR is first used to survey the line(s) (Figure 3a). Then, water infiltration and the nanotracers injection are conducted as described below.

Water inside the ring begins seeping into the soil once the plastic sheet is removed. At this point, the timer is started, recording the time taken for each centimeter of water level drop in the reservoirs, which corresponds approximately to 2 mm of water infiltrating through the ring. The GPR is then used to resurvey the line(s) (Figure 3b).

When the water level in the first reservoir reaches 0 cm (Figure 2, infiltration stage “c”), the GPR is again used to survey the designated line(s), marking the completion of the “infiltration function” characterization. Subsequently, the GPR surveys the line(s) as the second reservoir empties (Figure 3d). During this phase, for every 2 cm of water infiltrated (measured directly by the reservoir’s water level), 10 mL of SPIONs solution is injected into the ring. In total, 500 mL of SPIONs solution is injected, with a concentration of 3.35 g/L.

The infiltration experiment concludes when the water level in the second reservoir also drops to 0 cm (Figure 3e). At this point, all survey lines are scanned with the GPR.

Two GPR surveying strategies were utilized, involving distinct grid installation methods. The first strategy involved manually surveying a larger area (conducted in France). The second strategy aimed to enhance GPR data accuracy by automating the GPR displacement, focusing on a single survey line (conducted in Australia).

2.4.1 | GPR Strategy 1—French sites

The GPR system used in this study is the Geophysical Survey Systems Inc. SIR 3000, equipped with a 900-MHz antenna. In line with previous research (Di Prima et al., 2020), the 900-MHz antenna was selected to achieve a higher resolution of the top meter of soil, as the wavelength directly influences both measurement accuracy and penetration depth (Utsi, 2017). Higher frequencies limit the signal penetration depth but provide more precise details of radiowave propagation.

Two perpendicular survey lines were positioned around the ring (Figure 3II). Due to the placement of the reservoirs, additional survey lines could not be scanned during the test, which prevented following a full grid approach as done in Di Prima et al. (2020). Each survey line was 2 m long and marked at 20-cm intervals. To regulate the GPR’s speed and ensure proper signal acquisition, the time of arrival at each marker was recorded during the data collection process.

The GPR data, referred to as radargrams, were labeled as follows: "a" represents the dry state; "b" corresponds to the first reservoir's infiltration phase when only water is used; "c" indicates the intermediate stage when the first reservoir is empty; "d" refers to the second reservoir's infiltration, during which nanotracers are added inside the ring; and "e" denotes the final surveys, conducted after the completion of nanotracer injection (similar to Figure 3). When multiple surveys were conducted during the first or second reservoir infiltration, sequential numbers were appended to the letter, with the names presented in ascending order (e.g., d1, d2, d3).

2.4.2 | GPR Strategy 2—Australian sites

The GPR system used in this study was a PulseEKKO, equipped with a 1000-MHz antenna. This antenna was chosen to closely match the one used in Strategy 1 and to provide a high-resolution view of the top meter of soil, consistent with previous experiments.

A single survey line was followed by the GPR (Figure 3III) at a constant speed. A metal guide positioned above the GPR ensured stability and facilitated smooth movement. Manual labor was used to reposition the guide frame for each subsequent survey line.

To normalize the radargrams, three markers were incorporated into the data: one at the start of the transect (0 m), one at the midpoint (1 m), and one at the endpoint (2 m).

2.5 | GPR data processing and analysis

The GPR data are preprocessed using the same methodology as described in Di Prima et al. (2020). The radargrams were processed using the software ReflexW v4 (Sandmeier Geophysical Research). The steps involved are as follows: (1) importing the scan, (2) horizontally normalizing the data in distance (normalization between markers restricting the signal to the 0–2 m range), (3) removing the air–soil interface (t0), (4) reducing vertical noise using a filter (subtract-mean(dewow)), (5) applying a gain function to counter signal attenuation with depth, and (6) compressing the data by reducing the number of horizontal samples. The specific filters and parameter values are provided in the Supporting Information (Table S1). As recommended by Truss et al. (2007), the same values were applied consistently for all GPR data processing.

This step results in text files with four columns: X and Y (in meters), Z (in seconds), and G (amplitude of the signal). These columns define the simplified radargrams obtained over the full grid, where X and Y represent the distance between each survey line. The R software (The R Foundation) was then used to calculate the differences between two preprocessed radargrams.

To identify the wetted zones, the second stage of processing compares the treated radargrams of each survey line. It is assumed that portions of the radargrams will transition from an initial, water-free state to a final, water-filled state. The approach developed by Guo et al. (2014) and adapted by Di Prima et al. (2020, 2021, 2023) was used to compute the delineation of the state-changing portions of the survey lines. This method compares the distribution of absolute differences in values and considers amplitude variations. Large positive differences (due to the absolute value) indicate a state change, while small differences suggest no change in the local state. The threshold between nonsignificant and significant differences is set at 1.5 times the standard deviation of the distribution of differences (Di Prima et al., 2020). The region that shows a complete change when comparing the initial and final states corresponds to the infiltrated water zone. By default, the threshold is applied to the area at half the depth and below the ring.

We created text files for each radargram, preprocessed with ReflexW, containing the four previously mentioned columns. These files were used to generate tables with four columns: Z for depth (meters), X for easting (meters), Y for northing (meters), and the differenced amplitudes (G). The names of the two radargrams being compared are included in the name of the treated radargram files. For example, "|a-e|" refers to the outcome of thresholding and absolute differences between the "a" and "e" radargrams.

The comparison between water and nanotracer signals is performed using radargram visualizations. In R, differenced radargrams are plotted as heatmaps. The temporal evolution of the signal is assessed by comparing all radargrams over time with the first one: |a-b|, |a-c|, |a-d|, and |a-e| (with sequential numbers appended to the letters). These analyses are conducted for all nine tests, with Test 1 serving as a control, as only water was infiltrated during both phases.

2.6 | Nanotracers synthesis

The nanotracers were made of harmless natural minerals, that is, iron oxides for the core (magnetite, to be detectable with GPR), and silanes for the shell that covers the cores and functionalizes the surface (controlling the Zeta potential value). The challenge involved procuring nano-objects of a specific size (50–100 nm) and a fixed surface electric charge (with several targeted values), as well as ensuring the stability of the solution over time (to prevent the risk of aggregation and the formation of larger objects).

The synthesis of nanoparticles involves two main steps: the synthesis of the cores, followed by the formation of the silica shell. Briefly, $Fe(acac)_3$ precursors and triethyleneglycol are placed in a three-neck round-bottom flask equipped with a magnetic stirrer. For every 1 mmol of $Fe(acac)_3$, 12.5 mL of triethyleneglycol is required. The reactor was placed in a dry bath set to 180°C for 30 min; an aluminum foil was wrapped around the flask and its metal adapter for thermal insulation. Afterward, the temperature is quickly increased to 280°C, and the solution is maintained for 60 min. The heating system is then removed by lowering the laboratory jack, and the solution is allowed to cool to room temperature. Throughout the synthesis process, the flask is summited to argon flow for 1–2 min every 30 min, at a rate of 1 bubble per second.

The solutions are then purified three times by washing with ethyl acetate in a volumetric ratio of 1:3 and then stirred before being placed near a magnet to attract the particles and separate them from the solution. The initially black and opaque solution becomes clearer. This step is repeated until the final solution is transparent. At each step, the supernatant is extracted using a syringe while most of the particles remain agglomerated near the magnet. Once the solution is clear, it is centrifuged for 10 min at 1000 RPM to obtain the cores. The particles are then dried and stored at low temperature.

The second step involves silica coating with customized functionalization. Note that 62 mL of SPIONs are diluted in a mixture of 1 L of Triton X-100 (surfactant), 1 L of *n*-hexanol (co-surfactant), and 5 L of cyclohexane (oil phase). Mechanical stirring is set to 120 RPM, and the temperature is adjusted to approximately 40°C. Note that 16 mL of TEOS (tetraethoxysilane) is added to the solution, followed by 16 mL of catalyst (NH_4OH). After 72 h, 6 mL of specific silane is added to the solution. The silanes are chosen from three options: bis[(3-methyldimethoxysilyl)propyl]polypropylene oxide, *N*-(triethoxysilylpropyl)-O-polyethylene oxide urethane, Aquaphile AQ, and trimethoxysilylpropyl(poly ethyleneimine) hydrochloride. The solution is then left under stirring for an additional 72 h. The nanoparticles are subsequently precipitated via centrifugation and washed with acetone before being dispersed in water at the desired concentration. The final solution obtained is stored at room temperature.

The silica shell was designed to present different types of surface charge ranging from −10 to −30 mV under natural environments (pH between 5 and 9). All the objects were between 55 and 65 nm in diameter.

2.7 | Preliminary evaluation of nanotracer detectability using small rings

A small single-ring experiment was conducted on the Doua site to preliminarily test the hypothesis that there are signal differences between water and nanotracers. The experiment involved infiltrating 0.5 L of liquid into 5 cm-diameter rings (with a surface area of approximately 20 cm^2) under a variable head condition (i.e., the water level within the rings was not constant). A total of 18 rings were filled, with half containing water and the other half filled with nanotracers at their initial and maximum concentration (3.35 g/L).

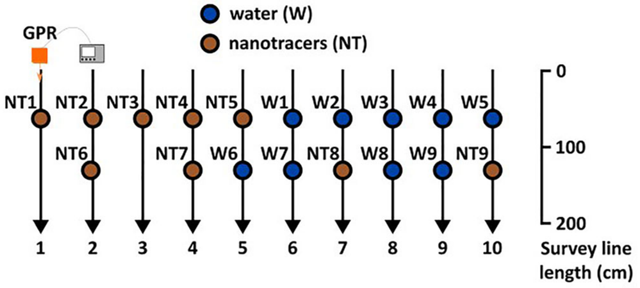

FIGURE 4 Localization of rings in the small single-ring experiment. Each ring is filled with either 0.5 L of water (W) or a nanotracer (NT) solution. Arrows indicate the direction of the ground-penetrating radar (GPR) survey. The length of the survey line is also specified.

The GPR surveyed the infiltrated areas along Lines 1–10, both before and after the injection of the liquids (Figure 4). The GPR data were then processed as described in subsequent sections. To facilitate detailed visualization, each survey line was divided into two segments during processing (0–1 m and 1–2 m), allowing separate analysis of the infiltrations corresponding to the two rings. Each transect is thus 1 m long.

2.8 | Modeling flow and solute transport

Predictive flow and solute transfer models were developed to estimate the shapes and positions of the "wetted" (associated with water infiltration) and "contaminated" (associated with nanotracer presence) areas in the field experiments. The purpose of these models is to illustrate potential outcomes, rather than provide a precise depiction of the experimental results. During the field experiments involving the dual-reservoir system, the models simulate an initial phase of water infiltration (and the injection of a nonreactive tracer). In the second phase, two solutes are injected: one reactive and the other nonreactive. The injection of the nonreactive solute either during or after the infiltration of the first reservoir helps to understand how the solute would behave without any reactivity. Modeling reactive versus nonreactive solutes further aids in understanding the effects of reactivity.

For this study, we employed the HYDRUS software, a tool specifically designed to simulate water flow and solute transport in variably saturated media across one-, two-, or three-dimensional (3D) domains (Šimůnek et al., 2016). HYDRUS numerically solves the Richards equation, which governs water flow in unsaturated conditions. The equations used for single-permeability soils under the assumption of axisymmetric water flow—commonly applied in infiltration experiments—are presented by Šimůnek et al. (1998):

$$\frac{\partial\theta}{\partial t} = \frac{\partial}{\partial z}\left(K(\theta)\left(1+\frac{\partial h}{\partial z}\right)\right) + \frac{1}{r}\frac{\partial}{\partial r}\left(rK(\theta)\frac{\partial h}{\partial r}\right) \quad (2)$$

Solving these equations requires hydraulic functions such as the water retention curve, $\theta(h)$, and the unsaturated hydraulic conductivity, $K(\theta)$. In HYDRUS, these relationships are represented using the van Genuchten (1980) model with Mualem's condition ($m = 1 - 1/n$) and capillary model (Mualem, 1976):

$$K\left(S_e\right) = K_s\, S_e^l\left(1-\left(1-S_e^{1/m}\right)^m\right)^2 \quad (3)$$

Solute transport in 3D is generally described by the advection-dispersion function (Equation 4) (Šimůnek & Genuchten, 2008).

$$\frac{\partial\theta c}{\partial t} + \rho\frac{\partial s}{\partial t} = \frac{\partial}{\partial z}\left(\theta D\frac{\partial c}{\partial z}\right) - \frac{\partial qc}{\partial z} - \phi \quad (4)$$

with θ [L^3L^{-3}] the water content, c [ML^{-3}] the solute concentration in solution, s [MM^{-1}] is the sorbed concentration, D [L^2T^{-1}] the dispersion coefficient accounting for both molecular and hydrodynamic dispersion, q[LT^{-1}] the Darcian fluid flux density, ϕ [$ML^{-3}T^{-1}$] is a sink-source term.

The sorption equation can be simplified in a linear form, depending on the distribution coefficient K_d [L^3M^{-1}]:

$$s = K_d\, c \quad (5)$$

The time is described by the Crank–Nicolson scheme, and the space by the Galerkin Finite Elements. The tortuosity is represented by the Millington and Quirk equation. The molecular diffusion coefficients in water and air are null. The reactive solutes have a distribution coefficient set to $K_d = 0.5\text{cm}^3/\text{M}$. The nonreactive tracers have a null distribution coefficient.

The simulations were performed using a 100 cm^2 numerical domain during 400 min (Figure 5). Water infiltration was modeled through a disc source with a diameter of 50 cm. Four soil configurations were simulated. The first configuration was a control soil consisting of homogeneous sandy loam. The second and third configurations included the same soil amended with a tortuous macropore, modified with high-permeability walls and low-permeability walls. The last configuration adds an impervious layer interrupting the macropore at a depth of 70 cm and measuring 14 cm. For the four configurations, the two phases (water only and then water combined with solutes) are modeled.

The hydraulic and transport properties were assigned as follows. The primary domain was composed of sandy loam, with parameters derived from Carsel and Parrish (1988). Macropores were characterized by hydraulic properties typical of coarse materials, exhibiting low capillarity and high saturated hydraulic conductivity. The macropore walls shared the same water retention parameters as the surrounding soil but had two values for saturated hydraulic conductivity: either a value slightly higher than the surrounding soil, which allowed unrestricted exchange, or a very low value, which blocked water exchange. The pathways of water flow were strongly influenced by the interaction between the macropores and the surrounding soil matrix, as described by Lassabatere et al. (2014). The impeding layer had the same retention parameters as the surrounding soil but was assigned a lower saturated hydraulic conductivity. The ring insert represented a 5-cm insertion into the soil with very low hydraulic conductivity. Further details of the hydraulic parameters can be found in Table 2.

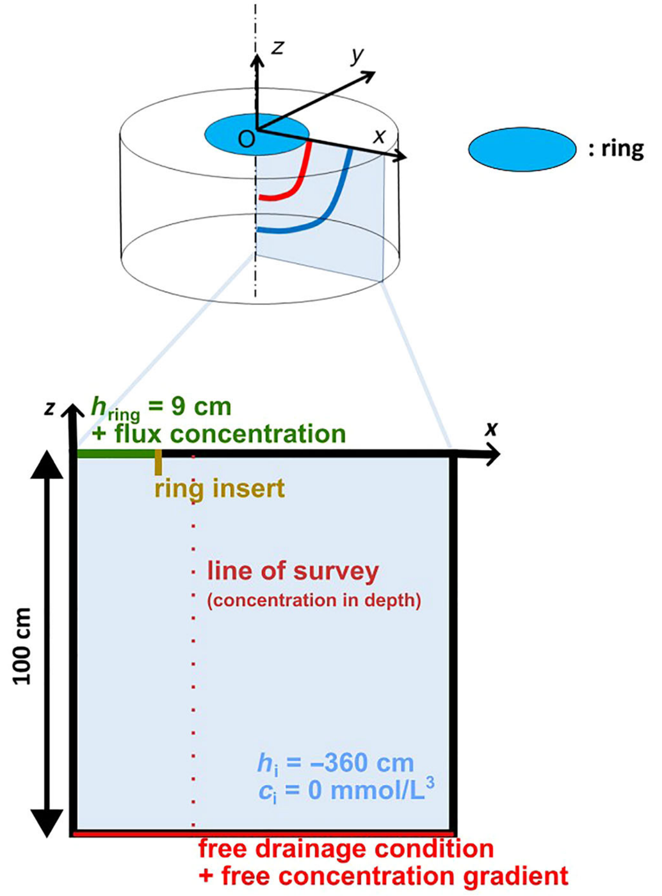

FIGURE 5 Scheme of the HYDRUS numerical domain and initial conditions.

The initial and boundary conditions were defined as follows. The entire domain was set to an initial pressure head of −360 cm for water content, representing the field capacity of the soil under investigation, and of 0 mmol/cm^3 for the initial concentration of the solute. A free-drainage condition (for water content) and a free concentration gradient (for solute transport, with a third-type condition) were applied to the bottom boundary. A pressure potential of 9 cm and a

TABLE 2 Hydraulic parameters used in HYDRUS for preliminary modeling of infiltration tests. The table specifies the hydraulic properties assigned to different soil components and structures, including the matrix (sandy loam), macropores, macropore walls, ring insert, and impeding layer.

	θ_r	θ_s	α (cm^{-1})	n (−)	K_s (cm/min)	l (−)
Soil (sandy loam)	0.065	0.41	0.075	1.89	0.074	0.5
Macropore	0	0,41	0.1	2	1	0.5
Macropore walls—low permeability	0	0.41	0.075	2	0.0001	0.5
Macropore walls—high permeability	0	0.41	0.075	2	0.1	0.5
Ring insert	0	0.41	0.075	2	0.00000003	0.5
Impeding layer	0	0.41	0.075	2	0.00005	0.5

flux concentration were imposed on the surface over the area corresponding to the radius of the ring at the top left of the domain.

An axisymmetric geometry was used in the model, as it is particularly well-suited for simulating water infiltration experiments with a disc source. However, this geometry results in toroidal volumes instead of rectangular cuboids. This introduces a bias when incorporating a macropore, as the model assumes the macropore forms a complete torus encircling the ring.

3 | RESULTS AND DISCUSSION

3.1 | Infiltration function

3.1.1 | Cumulative infiltration and infiltration rate

The cumulative infiltration and infiltration rate curves for all sites are shown in Figure 6. The cumulative infiltration curves exhibit a typical shape, characterized by an initial concave section followed by a more linear portion, corresponding to the transient and steady-state regimes of soil infiltration, respectively (Haverkamp et al., 1994; Smettem et al., 1994). These curves show that the infiltration function is directly influenced by the horizontal capillary forces (concavity part) and by gravity, which governs vertical infiltration. The infiltration rate curves also follow a characteristic pattern (an initial sharp decline followed by a more stable stage), consistent with the concave-linear shapes of the cumulative infiltration curves. The Burnley site exhibits significantly faster cumulative infiltration and infiltration rate compared to the other sites. This site had recently been restructured with coarse particles (mainly sand), leading to relatively large pore spaces between particles and minimal clogging. In contrast, for the ENTPE and IUT sites, which have sandy loam soils, no significant differences are observed in the infiltration curves. Overall, these results provide initial insights into the infiltration function of the studied soils.

3.1.2 | GPR for characterizing flow pathways

The GPR response to water-only infiltration during Test 1 is shown in Figure 7, presented by infiltration stage (first and second halves of the infiltration experiment) and by survey line (SLA [Survey Line A] and SLB [Survey Line B]). Differences between radargrams, highlighted by colored areas, indicate changes in water content and thus reveal flow dynamics as suggested by Di Prima et al. (2020). The color scale in the legend remains consistent across each survey line, allowing clear observation of the evolution of wetted zones (i.e., the colored areas).

Distinct patterns emerge depending on both the stage of infiltration and the survey line. For instance, increasing differenced amplitudes between Stages 1 and 2 are observed for SLA, indicating a progressive rise in water content under the GPR survey line (Figure 7, SLA, |c-e| vs. |a-c|). This trend is less evident for SLB. Additionally, darker patterns in SLA appear near the upper portion of the heat map, suggesting that the highest water content remains close to the surface at the end of the experiment. In contrast, water appears to have infiltrated more deeply for SLB. These radargrams demonstrate that flow pathways during the same infiltration experiment can vary significantly in space. Therefore, conventional surface measurements (such as cumulative infiltration and infiltration rate) are insufficient to fully characterize the infiltration function and flow pathways through the soil profile. More complex subsurface processes occur, which can be visualized using GPR. As suggested for heterogeneous soils, and in particular for dual-permeability soils, water infiltration experiments are indicative of the bulk capacity of soils to infiltrate and give no insight into the distribution of flow between fast flow and matrix flow (Lassabatere et al., 2014).

An initial hypothesis of this experiment was that steady-state conditions would be reached midway through the infiltration process. Under this assumption, the introduction of nanotracers during the second half would affect the GPR signal solely due to their presence. However, Figure 7 shows that changes in soil water content persist between Stages 1 and

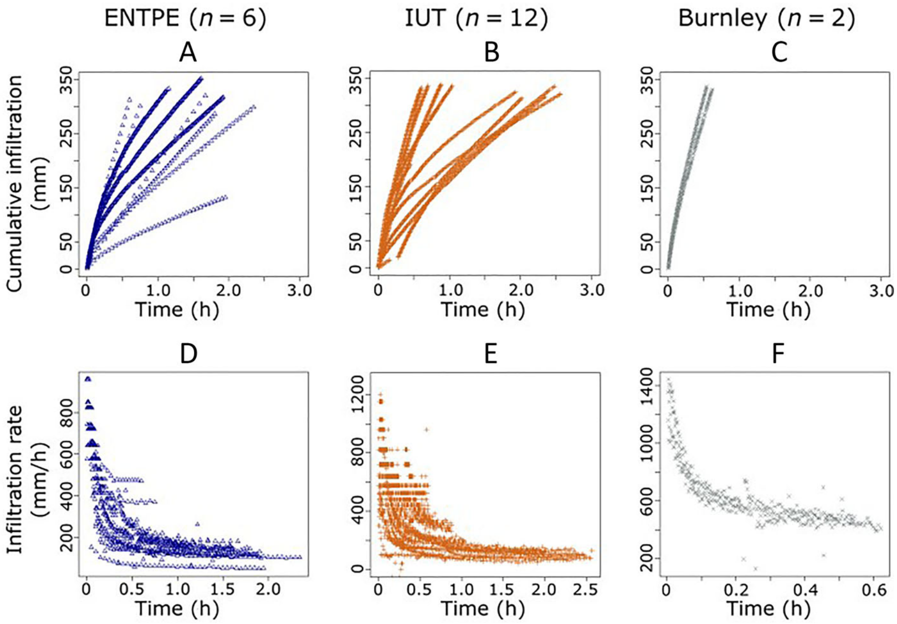

FIGURE 6 Cumulative infiltration (A–B) and infiltration rate (D–F) curves on the ENTPE (Engineering School of Sustainable Land Planning) site (A and D), on the IUT site (B and E), and on the Burnley site (C and F). The number of tests *n* is specified.

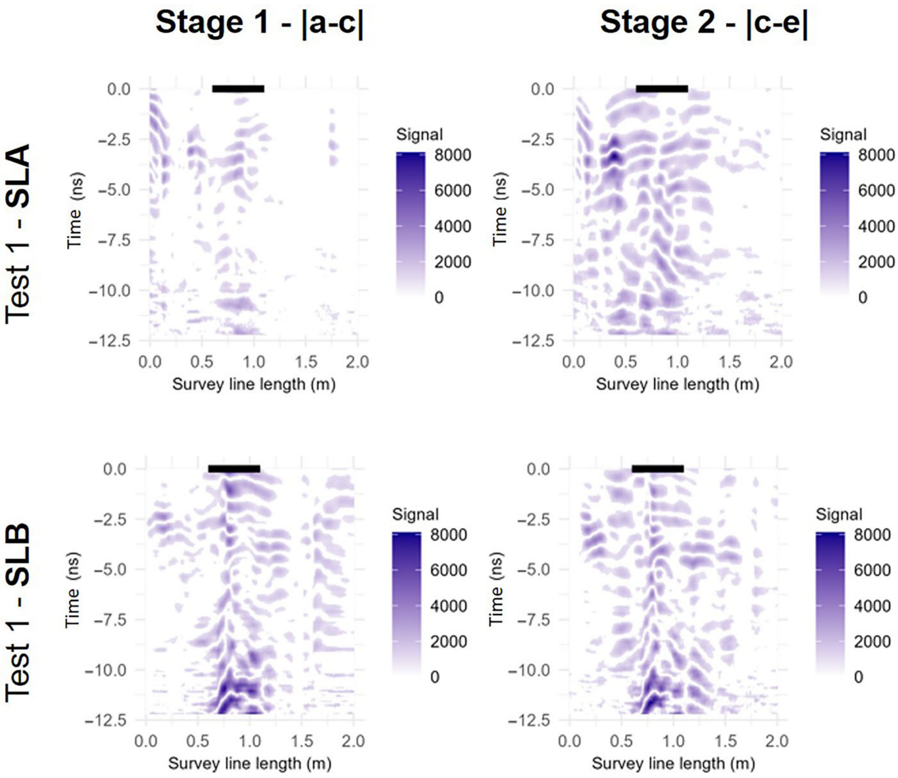

FIGURE 7 Visualization of Test 1 water injections for Stage 1 (|a-c|) and Stage 2 (|c-e|) at the ENTPE (Engineering School of Sustainable Land Planning) site. Differenced radargrams from Test 1 are presented for two survey lines: SLA (Survey Line A) and SLB (Survey Line B). Black lines indicate the ring's position.

2, indicating that a steady state was not yet achieved over this section. This highlights the need for caution when attributing changes in GPR signals during the second half of the experiment solely to nanotracers. While the assumption of distinct signal responses between water and nanotracers provides a useful simplification for tracer identification, it may not fully capture the complexity of actual infiltration dynamics.

3.2 | Filtration function

The detectability of SPIONs using GPR has been demonstrated at the highest possible SPIONs concentration (see Figures S1 and S2). This confirms the ability of GPR to distinguish between water-only and SPIONs-laden infiltration stages for high concentrations. The objective now is to characterize the filtration function by comparing signals after and before nanotracer injections.

Figure 8 presents visualizations of the "wetted" zones (in blue) associated with water infiltration and the "contaminated" zones (in red) associated with nanotracer presence. Signal intensity varies across tests and survey lines, making direct comparison of signal strength inadvisable.

Isolating or identifying "contaminated" regions to complete the filtration function assessment remains challenging. Specifically, there is no distinct transition or signal discontinuity making the boundary between "wetted" and "contaminated" zones as the experiment progresses from the first to the second infiltration stage. Various analyses (not shown here), along with the initial validation tests (Figures S1 and S2), suggest that nanotracers may slightly increase signal amplitude. However, the differences are neither visible nor statistically significant. The main difference with the validation test is the used concentration of nanotracers. In the tests presented here, the solution was diluted by a factor of 100. As a result, the variation in electromagnetic properties between the soil, water, and nanotracers is less pronounced, making it more difficult for GPR to distinguish the nanotracers. To conclude, signal variations observed in the second infiltration stage cannot be reliably attributed solely to the presence of nanotracers.

The variations in results between two radargrams (in general) may also be influenced by the transect locations and water flow paths. Note that GPR surveys are positioned around the ring and not directly below the infiltration area (see Figure 2). In some cases, water moves more slowly, often beneath the ring, causing the signal to continue increasing (even 20 min after stopping infiltration). In others, water diverges from the transects, either vertically or horizontally, reducing the signal. It is also hypothesized that for preferential flow paths with rapid infiltration, stopping the water supply at the surface deactivates these paths, leading to the disappearance of certain patterns and impacting the cumulative distribution of differentiated amplitudes. It is important to note that the scattering effect observed in the radargrams is directly related to the nature of the electromagnetic signal, which oscillates around zero. Thus, the values alternate between highly positive and highly negative, producing a scattered appearance. In contrast, 3D imaging of interpolated differentiated GPR data may improve data representation and visualization, helping to distinguish wetted zones during the monitoring of infiltration experiments (Di Prima et al., 2020). However, it requires elaborate processing protocols and a high number of survey lines, which reduces the frequency of data acquisition in time-lapse protocols, thereby lowering temporal resolution. In this study, and as mentioned above, the focus was put on the acquisition of enough transects in order to depict clearly the water flow dynamics.

From the visualization of the experimental differenced radargrams, distinct typologies of patterns can be identified. An example of each type of pattern is represented in Figure 8, and the other tests' radargrams can be found in Supporting Information S3 (Figures S3 and S4). For Test 3-SLA, the signal generally increases over time and depth. Most of the water appears to remain at greater depths. For Test 4-SLA, most of the signal is concentrated near the surface, and no real increase in the signal can be observed. For Test 5-SLA, there is a clear increase and enlargement of the signal in time, and at the end, the high amplitudes can be observed almost everywhere. For Test 5-SLB, the signal is restrained under the ring (black line), but in all the depth, with a columnar shape. Finally, for Test 8, a similar small columnar shape behind the surface ring appears (Figure 8) but can only be seen on the top of the graph (similar to Test 4-SLA). Signal variations are observed not only between the two survey lines within the same experiment but also between tests conducted in the same area, highlighting the inherent heterogeneity of field soils. Despite these challenges, the classification of "wetted" and "contaminated" regions offers valuable insights for improving the assessment of infiltration and filtration functions. This will be discussed in the following section.

3.3 | Comprehensive modeling of infiltration and filtration functions

Distinguishing between regions wetted by water and those reached by nanotracers is essential for the simultaneous characterization of infiltration and filtration processes. In this section, we use numerical modeling of flow and pollutant transport to simulate water content and nanotracers concentration maps across various soil types in order to (1) categorize flow patterns and (2) provide insights into the potential locations of nanotracers. This approach supports the identification and interpretation of areas classified as "wetted" (indicating water infiltration) and "contaminated" (indicating nanotracers

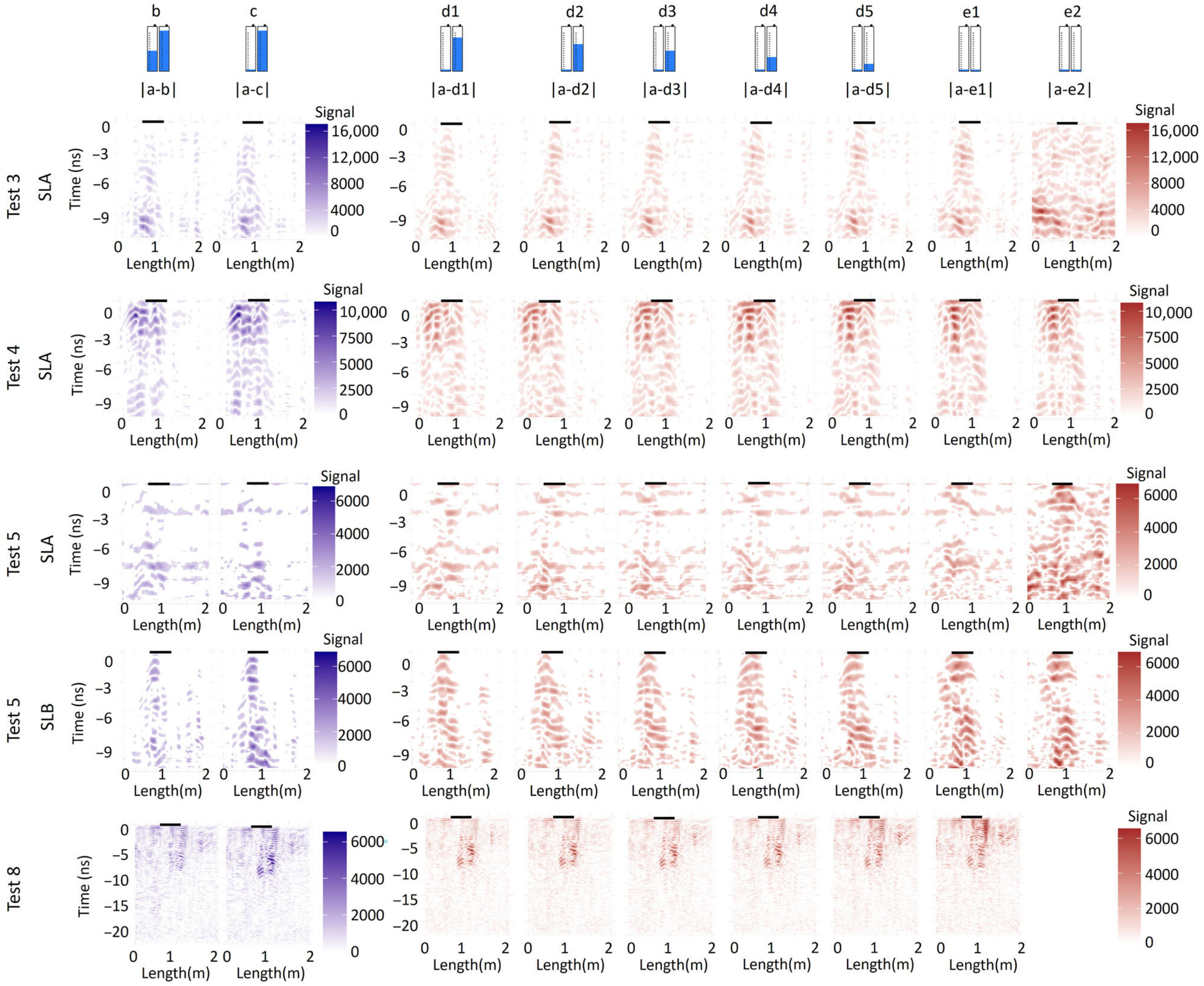

FIGURE 8 Visualization over time of radargrams, all differenced with the initial dry soil radargram (a). The radargrams are displayed in depth (ns) relative to length (m). Results are presented for ground-penetrating radar (GPR) Strategy 1—Test 3 (Survey Line A), Test 4 (Survey Line A), and Test 5 (Survey Lines A and B), and for GPR Strategy 2—Test 8. The left graphs (shades of blue) correspond to water infiltration, while the remaining radargrams (shades of red) represent the injection of the nanotracers solution. Black lines indicate the ring's position.

presence), which is particularly relevant for interpreting GPR data. Simulations are conducted under four scenarios: (1) homogeneous soil, (2) soil with a macropore with highly permeable walls, (3) soil with a macropore with low-permeability walls, and (4) soil with an impervious layer at depth.

3.3.1 | Infiltration function—Water flow

The infiltration results are presented in Figure 9 through various graphs for each scenario. They are first shown as water content maps at two infiltration times (200 and 400 min), corresponding to the middle and the end of the infiltration experiment (Figure 9—Columns 2 and 3). The water content profiles are also given at the location of the GPR Survey Line (Column 4). We remind that GPR survey lines are positioned 10 cm beside the ring (see Figure 2) and are indicated as the black line in Figure 9 (Columns 1–3). Thus, we note that the water content maps (Columns 2 and 3) are presented over the *x*–*z* plane, and the water content (Column 4) is shown at the intersection of the *x*–*z* plane and the *y*–*z* plane. The survey line follows the *y*-axis at the black vertical line position (*x*-axis). The water content (Column 4) helps infer the shapes and intensity of the "wetted" and "contaminated" zones beneath the GPR survey lines. Consequently, the shapes corresponding to zones of expected increasing contrast, based on a hypothesized differentiation between the initial and final radargrams (|a-e|), are shown (Columns 5–6). The analysis of the correspondence between inferred shape and modeled processes will help infer processes from acquired GPR survey lines under real conditions and distinguish "wetted" from "contaminated" zones.

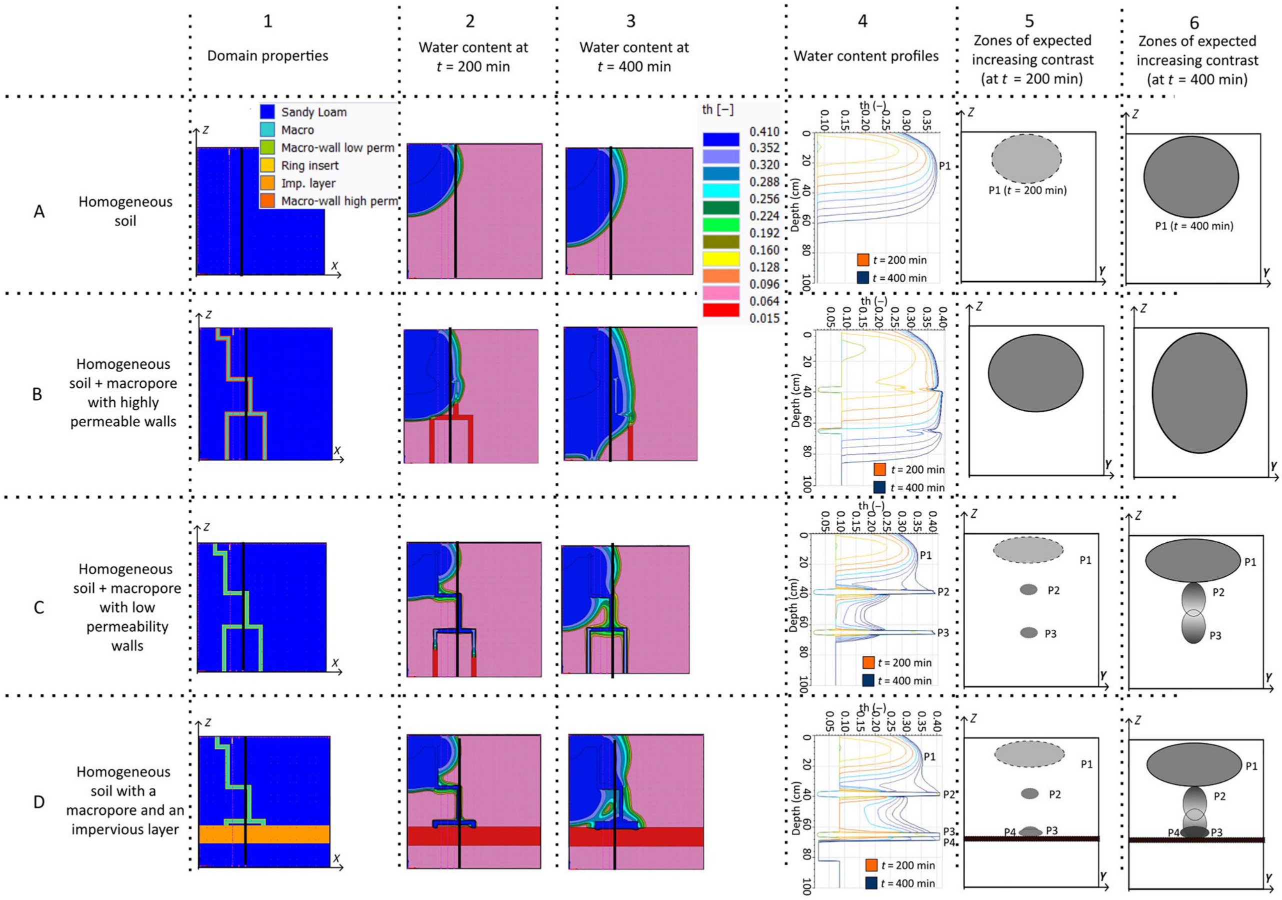

FIGURE 9 Modeling of different soil types: homogeneous (A), macroporous (B and C), and macroporous with an impermeable layer (D). The difference between B and C lies in the permeability of the macropore walls: high permeability for B and low permeability for C. For all these soil types, the following are presented: 1, the numerical domain; 2, water content at $t = 200$ min; 3, water content at $t = 400$ min; 4, water content profiles over time; 5, zones of expected increasing contrast at $t = 200$ min; 6, zones of expected increasing contrast at $t = 400$ min.

In homogeneous soil, the infiltration front assumes a bulbous shape, progressing vertically due to gravity and spreading horizontally due to capillarity (Figure 9 Line A, Column 2, Line A Column 3). By analyzing the water content profile, some areas extending both vertically and horizontally are anticipated for the shape of the wetted zone beneath the GPR survey line, as depicted in Figure 9 Line A Column 5 (P1). This pattern resembles that observed during the infiltration of Test 4-SLA (Figure 8).

In soil with a macropore network and highly permeable walls, water exchange between the macropore network and the surrounding matrix is more efficient (Figure 9 Line B). This rapid exchange leads to the saturation of the surrounding matrix, forming an infiltration bulb around the macropore network. Water content maps suggest a single infiltration bulb in the matrix, albeit with quicker displacement and shape distortion. These findings are consistent with the results of Lassabatere et al. (2014) who also explored water infiltration in dual-permeability soils. At $t = 200$ min, the concentration profile shows two distinct zones, the infiltration bulb (P1) and the upper macropore network (P2), which are not anymore differentiable at $t = 400$ min. The profile line intersects the wetted zone across almost the entire depth. As a result, the differentiated radargrams would have at $t = 400$ min nearly all of their area surveyed with high signal values, transitioning from dry to nearly completely wet soil vertically. Such a scenario could be difficult to distinguish from the homogeneous scenario in a very permeable soil, unless the distortion of the bulb is evident enough.

In soils with a macropore network and limited water exchange between macropores and the surrounding matrix (due to low-permeability walls), water content maps reveal preferential flow along the macropore network. These flows create distinct wetted zones with isolated flow pathways. The profile line intersects both matrix infiltration and the two flow pathways within the macropore network (Figure 9 Line C Column 2, Line C Column 3). The water content profile (Figure 9 Line C Column 4) shows three distinct zones: the infiltration bulb (P1), the upper macropore network (P2), and the lower macropore network (P3). Water reaches the points P1 and P2 almost at the same time (not visible on Figure 9), suggesting that changes in the GPR radargram could appear together at P2 and P1 (or maybe P2 before P1, if the hydraulic conductivity of the macrospore is even higher), which seems counterintuitive. However, the flow logically proceeds from P2 to P3. Extrapolating the water profiles to the entire vertical section below the GPR survey line could result in the visualization of three distinct shapes at P1, P2, and P3, along with larger matrix bulbs, as shown in Figure 9 (C-5) at 200 min and (C-6) at 400 min. The patterns observed in both types of macroporous soils (with highly or low-permeability walls) resemble those of the infiltrations in Test 5-SLB and Test 8 (Figure 8). However, the GPR method is not precise enough to determine the macropore size.

The presence of an impeding layer in the soil further impacts water content, flow pathways, and the movement of infiltration bulbs. When water encounters the impeding layer, infiltration ceases, leading to water accumulation above the impeding layer. This can form a perched aquifer, a phenomenon that has been studied in the context of funneled flow in heterogeneous soils with capillary barriers (e.g., Ben Slimene et al., 2017). A comparison of soils with and without an impeding layer shows similar water content at 200 min (Figure 9 Line D Column 2 vs. Line C Column 2). By 400 min, water penetrates below 80 cm in the absence of the layer, while in the presence of the impeding layer, it accumulates above the layer, resulting in better moistening of the upper soil (Figure 9 Line D Column 3 vs. Line C Column 3). In terms of water retention profiles, the impeding layer prevents deeper infiltration, forming a perched aquifer that moistens the profile from below, leading to water appearance at Point P4 (Figure 9 Line D Column 4). The expected GPR profiles in Figure 9 Line D Coumn 4) evolve over time, initially resembling that of the macropored soil without a layer before water appears at P4. Subsequently, a vertical layer (P4) forms, extending upward and appearing beneath the elliptical shapes (P1, P2, P3). The pattern associated with the impeding layer resembles the infiltration behavior observed in Test 3-SLA and Test 5-SLA (Figure 8). Infiltration appears to be more concentrated at depth in Test 3, possibly due to a macropore facilitating faster water movement compared to Test 5.

The different types of flow dynamics modeled could help characterize the variations observed in the radargrams from the same water infiltration experiments, thereby providing a more comprehensive characterization of the infiltration function. These modeled dynamics are (i) matrix flow involving larger volumes but slower displacement (Figure 9 Line A Column 2, Line A Column 3), and (ii) preferential flow, characterized by rapid increases in both water content and tracer concentration within the macropores (Figure 9 Lines B-D; Columns 2-3). A radargram with signals near the top may indicate a homogeneous soil with matrix flow; column-shaped patterns could result from macropores and preferential flow below the ring or flow in very permeable soils (not modeled here); and deeper patterns may be associated with impervious layers.

3.3.2 | Filtration function—Reactive and nonreactive solutes

The solute transport results are presented in Figure 10 through various graphs for each scenario. The transport of solutes beginning at the midpoint of the experiment ($t = 200$ min) is presented as concentration maps at $t = 400$ min, corresponding to the end of the infiltration phase. The concentration profiles are provided at the location of the GPR survey line, represented by a black line in Figure 10 (Columns 1, 2, and 5). The shapes corresponding to zones of expected increasing contrast, based on a hypothesized differentiation between the initial and final radargrams (|a-e|), are shown (Columns 4 and 7). By comparing the patterns and colors, these visuals can help infer the potential “contaminated” zones that would be detected by a GPR. Two types of solutes are modeled: one nonreactive (Figure 10, Columns 2–4) and the other reactive (Figure 10, Columns 5–7).

In homogeneous soil, the concentration front exhibits a bulbous shape, progressing vertically and spreading horizontally (Figure 10 Line A Column 2, Line A Coumn 5). The tracer follows the water flow, which defines itself as a bulbous shape progressing vertically due to gravity and horizontally due to capillarity (as described above). In other words, similar shapes are expected for water and tracer transport. The reactive solute forms a less extensive bulb compared to the nonreactive solute, which results from the delay due to its reactivity. The concentration profiles for both solutes display a single peak at the surface of the modeled domain. Notably, the reactive concentration bulb has not yet reached the GPR survey line (black line, Figure 10 Line A Column 5), which implies an absence of signal variation and no detectable feature in the expected GPR data. The peak profile has really low concentration values. For the nonreactive solute, the single peak indicates a small area of signal amplitude variation for the GPR (Figure 10 10 Line A Column 4). Such results show that even if some solutes are injected, depending on their reactivity, the solutes may not appear or be detectable using GPR. It should be noted that other chemical processes affecting reactive solutes (e.g., degradation, precipitation) were not modeled, although they may contribute to pollutant attenuation.

In soils with a macropore network and highly permeable walls, solutes are more efficiently distributed within the soil (Figure 10 Line B Column 2, Line B Column 5). The rapid exchange of the nonreactive solute between the sandy loam matrix and the macropore leads to water saturation and solute contamination of the surrounding matrix, forming infiltration and concentration bulbs around the macropore network. For the reactive solute, the concentration path is more confined to the macropore, with limited propagation to the surrounding matrix, again as the result of the delay imposed by its reactivity. The concentration maps again suggest a single bulb in the matrix; however, at the GPR survey line, the nonreactive solute shows a double peak in the concentration profile,

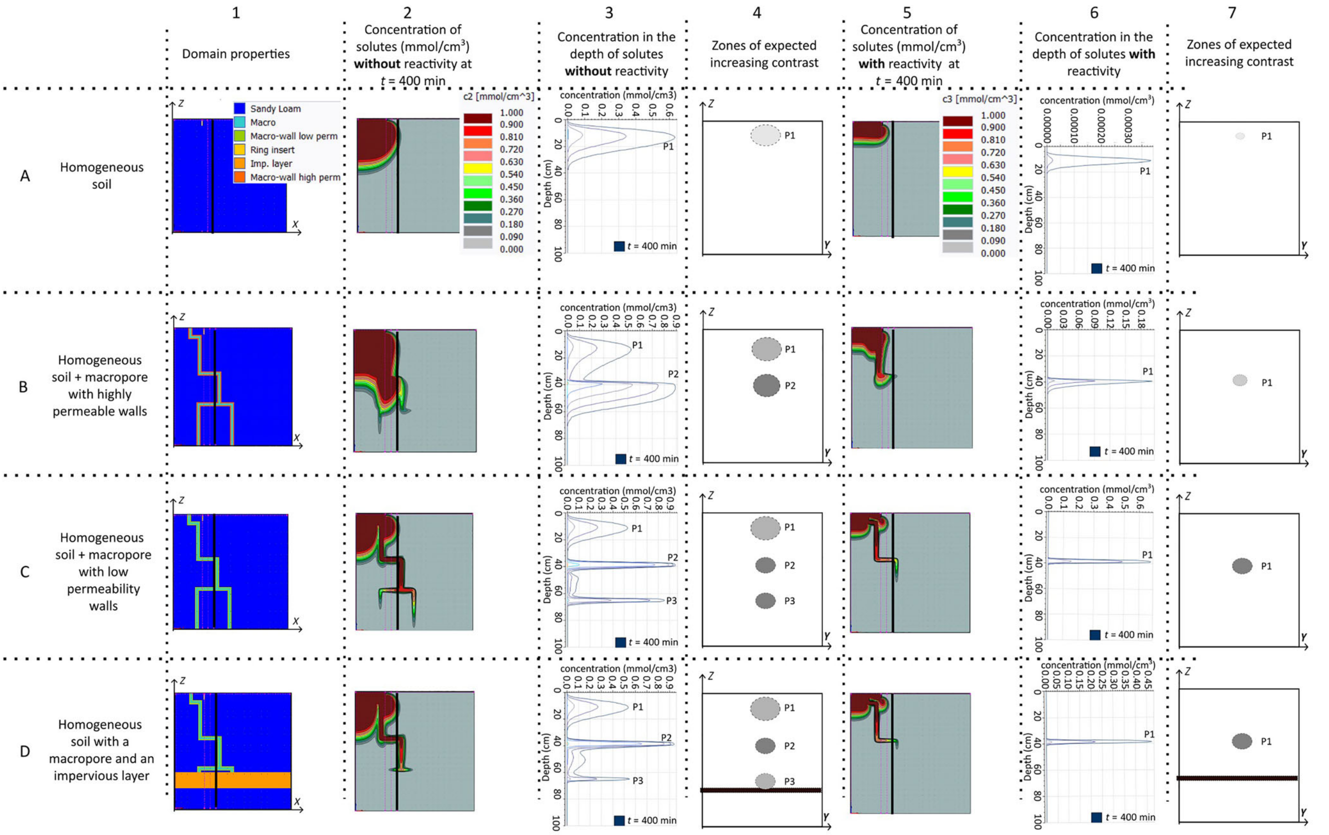

FIGURE 10 Modeling of different soil types: homogeneous (A), macroporous (B and C), and macroporous with an impermeable layer (D). The difference between B and C lies in the permeability of the macropore walls: high permeability for B and low permeability for C. For all these soil types, the following are presented: 1, the numerical domain; 2, concentration of solutes (mmol/cm^3) without reactivity ($K_d = 0\text{cm}^3/\text{M}$) at $t =$ 400 min; 3, concentration of nonreactive solutes profiles over time; 4, zones of expected increasing contrast; 5, concentration of solutes (mmol/cm^3) with reactivity ($K_d = 0.5\text{cm}^3/\text{M}$) at $t = 400$ min; 6, concentration of reactive solutes profiles over time; 7, zones of expected increasing contrast. The solute transport started at $t = 200$ min, after infiltrating only water for 200 min. The scales are not the same on the plots of concentration in depth.

reflecting the macropore's shape. This suggests that while some exchange occurs between the matrix and the macropore, the majority of solute transport follows the macropore, as observed for water. Reactivity introduces a transport delay but does not alter the overall path over time. The GPR response is expected to differ between the two solutes, with a double peak for the nonreactive solute and a single, deeper peak for the reactive solute (Figure 10 Line B Column 4, Line B Column 7). However, acquisition at larger times would also lead to double peaks for the slowest reactive solute. The time of acquisition is then crucial, and several transects must be sampled at several times to get a proper image of the dynamics of water flow and solute propagation with adaptation for slower reactive solutes.

In soils with a macropore network but low-permeability walls, solution exchange is more limited. The concentration maps reveal preferential flow along the macropore network, with both solutes following similar pathways, but the nonreactive solute lagging behind. Limited exchange between the matrix and the macropore network allows the solutions to penetrate deeper into the soil. Since the macropore shifts slightly away from the GPR survey line, part of the concentration profile is not captured, resulting in reduced information in the expected GPR data. While a large concentrated area is observed in the maps (Figure 10 Line C Column 2), the GPR profiles only show two distinct peaks (P2 and P3) in depth (Figure 10 Line C Column 3, Line C Column 4), appearing disconnected. The GPR patterns would thus be similar to those expected from the water infiltration stage.

On the previous results, two different strategies for the assessment of the filtration function may be considered: (i) comparing changes in the GPR signal resulting from the replacement of water with a solution containing nonreactive nanotracers and (ii) comparing two nanotracers with different reactivities. Strategy (i) involves analyzing the difference between the GPR signal obtained with the (nonreactive) tracer solution and that obtained with water. In this case, the nonreactive nanotracer is transported by convection and dispersion, with convection presumably being the dominant mechanism. We therefore expect a similar pattern to that observed with water alone (Figure 9). Although the tracer moved more slowly than water and reached the GPR survey line to a lesser extent, the main pattern features were preserved. With longer acquisition times, similar patterns would likely have emerged. This difference is attributable to two factors: (i) water infiltrates faster initially due to higher hydraulic gradients compared to the tracer solution, and (ii) the average pore velocity of nonreactive solutes is equal to the water flux divided by porosity, making it lower than the water flux itself. Consequently, the "contaminated" zone is expected to be more centralized and smaller than the "wetted" zone. It gives the feeling that under the current experimental setup, the detection of preferential flow is less evident for the "contaminated" zone (see Figure 10, Columns 4 and 7, vs. Figure 9, Column 6). These results are consistent with our experimental observations, where similar features were identified for both the nanotracer and water infiltration. The filtration function can thus be characterized by comparing GPR signals before and after replacing water with a solution containing nonreactive nanotracers.

Regarding Strategy (ii), the comparison between the simultaneous injection of two solutes (one nonreactive and the other reactive) can provide insights into the delay affecting the transport of the reactive solute. The numerically generated data clearly show that the reactive tracer lags behind the nonreactive tracer. Although this approach was not experimentally applied in this study, the simultaneous use of nanotracers with contrasting reactivities could offer valuable information on the transport behavior of different nanotracers in heterogeneous soils. Alternative injection protocols for solutes and nanotracers (e.g., varying injection timing, using different sets of nanotracers) could be explored to enhance differentiation between nanotracers and to quantify propagation delays. Such insights would help assess solute reactivity, particularly adsorption by the soil, thereby providing information on pollutant retention and enabling a more detailed characterization of the soil's filtration function. In any case, the use of GPR appears promising for monitoring the pathways of reactive solutes and comparing them with those of nonreactive solutes, providing insights into the filtration function.

The filtration function can thus be evaluated by monitoring the nanotracers, primarily through comparisons between different experiments or models. However, we encountered challenges in clearly identifying suitable indicators to assess tracer filtration and transport, as isolating the nanotracer signal from that of water proved difficult. One potential improvement would be to determine a "retardation time" between water and nanotracers or to use geometrical parameters to track nanotracer movement and filtration.

More broadly, the numerical modeling is intended to aid in understanding the processes underlying the different patterns observed in the actual radargrams, rather than to perfectly replicate real-world conditions. For example, the scattered appearance seen in the radargrams is not present here, as this is flow and transport modeling, not GPR signal modeling. In reality, field soils are rarely homogeneous or characterized by a single large macropore. Instead, they are much more complex. Nonetheless, this modeling provides a first insight into simplified, theoretical processes.

4 | LIMITS OF THE STUDY

INFILTRON-Exp proved to be an efficient tool for obtaining meaningful results in the estimation of the bulk infiltration capacity of soils, as well as for providing relevant information on the pathways of water and nanotracers. However, this distinction depends on having sufficient contrast between water and the nanotracer solution in terms of their electromagnetic wave propagation properties. This requirement introduces a limitation to the method.

Indeed, our experimental results showed that the simultaneous water infiltration and nanotracer injection followed by GPR may lack the precision to distinguish water and nanotracer signals. This limitation likely stems from the low concentration of nanotracers and the continued infiltration of water during the nanotracer injection. Furthermore, steady-state conditions are not reached by the end of the water injection stage, leaving the soil unsaturated. Consequently, changes in the soil's electromagnetic properties are influenced not only by the nanotracers but also by ongoing soil moistening, complicating (i) exclusive detection by GPR of the nanotracers from water and (ii) the determination of the precise transport and filtration behavior of the nanotracer. The same lack of precision would have rendered it complicated to distinguish two solutes of different reactivities injected at the same time. Further research must be conducted to optimize the protocol of injection of reactive versus nonreactive nanotracers in order to facilitate the detection of the nanotracers.

Once the method for the localization of nanotracers has been established, indicators of nanotracer velocity and dispersion will be developed to better characterize their movement and the retardation caused by filtration. Then, INFILTRON-Exp will be deployed to investigate various nanotracers with different surface charges (e.g., negative or positive) in order to simulate a broader range of pollutant behaviors. However, the SPIONs solutions currently used are quite expensive (approximately €200 per liter), which remains a limitation that could be addressed in future developments.

In terms of optimization of the acquisition of GPR, we investigated two strategies: (i) sampling two survey lines with an operator—French sites—or (ii) having a very accurate acquisition of one survey line. Both GPR strategies seemed to yield similar results. For improved accuracy, we recommend using an automated system to minimize potential human errors or employing a cart system as adopted, for instance, by Di Prima et al. (2023) and Stephan et al. (2024). At this stage, defining reliable parameters or indicators remains challenging due to these shortcomings. In addition, further research may be conducted regarding the nonintrusive technique used to detect the nanoparticles.

Finally, factors beyond soil heterogeneity such as physicochemical properties also influence these functions but are not addressed in this study and should be considered in future research.

5 | CONCLUSION

Infiltration and filtration are key soil functions, essential for assessing cities' vulnerabilities to water-related risks (such as flooding) and groundwater contamination. However, current methodologies often lack sufficient subsurface information and fail to provide a clear understanding of processes occurring beneath the soil surface. This study examines the INFILTRON-Exp infiltration experimental setup and protocols, specifically designed to quantify and qualify these functions more comprehensively. In addition to monitoring surface water fluxes, it offers relevant information on the subsurface pathways of water and nanotracers. INFILTRON-Exp integrates GPR and data processing algorithms and models to detect flow and nanotracer movement in the soil.

INFILTRON-Exp proved to be effective in quantifying the soil's infiltration capacity and in revealing the pathways of water and nanotracers underground. The results highlight the value of GPR imaging in improving the assessment of infiltration and filtration functions, especially given that traditional parameters (such as cumulative infiltration) are insufficient on their own. To support this assessment, a numerical study was conducted to simulate different flow types across varying soil heterogeneities, including homogeneous soils (matrix flow), macropores (preferential flow), and impervious layers. Modeling was instrumental in interpreting the processes at play and in linking GPR signals to observed water and nanotracer pathways. These numerical results were then used to help interpret field observations.

Altogether, this study presents both a novel device and a novel method for characterizing infiltration and filtration functions. INFILTRON-Exp represents a promising first step. Compared to other field methods, INFILTRON-Exp is easier to use, faster, and nondestructive. Its larger size allows for better representation of natural soil conditions, thereby reducing the number of experiments required. Moreover, the device is adaptable to a range of soil types (not just urban soils), including coarser soils, by placing a layer of bentonite between the soil and the ring to prevent water leakage.

Further advancements are needed to improve INFILTRON-Exp, particularly regarding the detection of nanotracers in the soil. Two main research directions are proposed to address this issue: (i) improving the detectability of nanoparticles and (ii) enhancing the selection and application of nonintrusive techniques for subsurface detection. Preliminary studies on nanotracer design suggest that using only natural, nontoxic minerals for SPIONs limits the ability to create highly contrasting tracers (INFILTRON project, www.infiltron.org). As for detection methods, alternative approaches such as electrical resistivity tomography (ERT) may offer more robust solutions for monitoring SPION injections. ERT has already been successfully applied to detect water pathways in infiltration systems (Delgado-Gonzalez et al., 2023; Louis et al., 2024) and appears promising for detecting electrically responsive tracers. Future work will explore the potential of this technique.

AUTHOR CONTRIBUTIONS

Gersende Fernandes: Conceptualization; data curation; formal analysis; investigation; methodology; visualization; writing—original draft; writing—review and editing. **Simone Di Prima**: Conceptualization; methodology; software; validation; writing—review and editing. **Gislain Lipeme Kouyi**: Conceptualization; funding acquisition; project administration; supervision; writing—review and editing. **Tim D. Fletcher**: Funding acquisition; investigation; supervision; writing—review and editing. **Daniel Donze**: Conceptualization; investigation. **Robert James**: Conceptualization; investigation; writing—review and editing. **Saint-Martin Saint-Louis**: investigation. **Matteo Martini**: Conceptualization; methodology; writing—review and editing. **Claudia Nicklason**: Investigation. **Laurent Lassabatere**: Funding acquisition; investigation; methodology; project administration; supervision; validation; writing—review and editing.

ACKNOWLEDGMENTS

We are deeply grateful to Dr. Rafael Angulo-Jaramillo and Dr. Thierry Winiarski for their guidance in the field and their contributions to data interpretation. We also thank Professors Vincenzo Bagarello and Massimo Iovino for their participation in the INFILTRON project, which enabled us to explore the concepts of infiltration and filtration functions. Funding for this study was provided by (i) the INFILTRON project, supported by the French National Research Agency (ANR-17-CE04-010), and by (ii) the French Ministère de l'Environnement. This work was also carried out with the support of the EUR H2O'Lyon (ANR-17- EURE-0018) of the University of Lyon (UdL) as part of the "Investissements d'Avenir" program managed by the French National Research Agency (ANR) and performed in part within the framework of the OTHU (Field Observatory for Urban Water Management—http://othu.org). Fletcher is supported by an Australian Research Council Industry Laureate Fellowship (ARC IL230100020).

CONFLICT OF INTEREST STATEMENT

The authors declare no conflicts of interest.

ORCID

Gersende Fernandes https://orcid.org/0000-0001-7419-7377
Simone Di Prima https://orcid.org/0000-0002-5066-3430
Laurent Lassabatere https://orcid.org/0000-0002-8625-5455

REFERENCES

Alaoui, A., Caduff, U., Gerke, H. H., & Weingartner, R. (2011). Preferential flow effects on infiltration and runoff in grassland and forest soils. *Vadose Zone Journal*, *10*, 367–377. https://doi.org/10.2136/vzj2010.0076

Allaire, S. E., Roulier, S., & Cessna, A. J. (2009). Quantifying preferential flow in soils: A review of different techniques. *Journal of Hydrology*, *378*, 179–204. https://doi.org/10.1016/j.jhydrol.2009.08.013

Angulo-Jaramillo, R., Bagarello, V., Iovino, M., & Lassabatere, L. (2016). *Infiltration measurements for soil hydraulic characterization*. Springer. https://doi.org/10.1007/978-3-319-31788-5

Angulo-Jaramillo, R., Vandervaere, J.-P., Roulier, S., Thony, J.-L., Gaudet, J.-P., & Vauclin, M. (2000). Field measurement of soil surface hydraulic properties by disc and ring infiltrometers. A review and recent developments. *Soil and Tillage Research*, *55*, 1–29. https://doi.org/10.1016/S0167-1987(00)00098-2

Aryal, R., Vigneswaran, S., Kandasamy, J., & Naidu, R. (2010). Urban stormwater quality and treatment. *Korean Journal of Chemical Engineering*, *27*, 1343–1359. https://doi.org/10.1007/s11814-010-0387-0

Ben Slimene, E., Lassabatere, L., Simunek, J., Winiarski, T., & Gourdon, R. (2017). The role of heterogeneous lithology in a glaciofluvial deposit on unsaturated preferential flow—A numerical study. *Journal of Hydrology and Hydromechanics*, *65*, 209–221. https://doi.org/10.1515/johh-2017-0004

Bünemann, E. K., Bongiorno, G., Bai, Z., Creamer, R. E., De Deyn, G., de Goede, R., Fleskens, L., Geissen, V., Kuyper, T. W., Mäder, P., Pulleman, M., Sukkel, W., van Groenigen, J. W., & Brussaard, L. (2018). Soil quality—A critical review. *Soil Biology and Biochemistry*, *120*, 105–125. https://doi.org/10.1016/j.soilbio.2018.01.030

Carsel, R. F., & Parrish, R. S. (1988). Developing joint probability distributions of soil water retention characteristics. *Water Resources Research*, *24*, 755–769. https://doi.org/10.1029/WR024i005p00755

Chéry, L., & Mouvet, C. (2000). Main physico-chemical and biological processes in pollutants percolation and their transfer towards groundwater. *La Houille Blanche*, *86*, 82–88. https://doi.org/10.1051/lhb/2000079

Citeau, L. (2008). *Transfert eaux-sols-plantes de micropolluants: état des connaissances et application aux eaux de ruissellement urbaines*. https://www.eau-seine-normandie.fr/domaines-d-actions/etudes/06PLUV07

Concialdi, P., Di Prima, S., Bhanderi, H. M., Stewart, R. D., Abou Najm, M. R., Lal Gaur, M., Angulo-Jaramillo, R., & Lassabatere, L. (2020). An open-source instrumentation package for intensive soil hydraulic characterization. *Journal of Hydrology*, *582*, Article 124492. https://doi.org/10.1016/j.jhydrol.2019.124492

Delgado-Gonzalez, L., Forquet, N., Choubert, J.-M., Boutin, C., Moreau, M., Moreau, S., & Clement, R. (2023). Flow path monitoring by discontinuous time-lapse ERT: An application to survey relationships between secondary effluent infiltration and roots distribution. *Journal of Environmental Management*, *326*, Article 116839. https://doi.org/10.1016/j.jenvman.2022.116839

Di Prima, S. (2015). Automated single ring infiltrometer with a low-cost microcontroller circuit. *Computers and Electronics in Agriculture*, *118*, 390–395. https://doi.org/10.1016/j.compag.2015.09.022

Di Prima, S., Fernandes, G., Marras, E., Giadrossich, F., Stewart, R. D., Abou Najm, M. R., Winiarski, T., Mourier, B., Angulo-Jaramillo, R., Comegna, A., del Campo, A., & Lassabatere, L. (2023). Evaluating subsurface flow connectivity in a pine-covered hillslope with stemflow infiltration and ground-penetrating radar surveys. *Journal of Hydrology*, *620*, Article 129527. https://doi.org/10.1016/j.jhydrol.2023.129527

Di Prima, S., Giannini, V., Roder, L. R., Giadrossich, F., Lassabatere, L., Stewart, R. D., Abou Najm, M. R., Longo, V., Campus, S., Winiarski, T., Angulo-Jaramillo, R., del Campo, A., Capello, G., Biddoccu, M., Roggero, P. P., & Pirastru, M. (2021). Coupling time-lapse ground penetrating radar surveys and infiltration experiments to characterize two types of non-uniform flow. *Science of the Total Environment*, *806*, Article 150410. https://doi.org/10.1016/j.scitotenv.2021.150410

Di Prima, S., Lassabatere, L., Bagarello, V., Iovino, M., & Angulo-Jaramillo, R. (2015). Testing a new automated single ring infiltrometer for Beerkan infiltration experiments. *Geoderma*, *262*, 20–34. https://doi.org/10.1016/j.geoderma.2015.08.006

Di Prima, S., Winiarski, T., Angulo-Jaramillo, R., Stewart, R. D., Castellini, M., Abou Najm, M. R., Ventrella, D., Pirastru, M., Giadrossich, F., Capello, G., Biddoccu, M., & Lassabatere, L. (2020). Detecting infiltrated water and preferential flow pathways through time-lapse ground-penetrating radar surveys. *Science of the Total Environment*, *726*, Article 138511. https://doi.org/10.1016/j.scitotenv.2020.138511

Gerke, K. M., Sidle, R. C., & Mallants, D. (2015). Preferential flow mechanisms identified from staining experiments in forested hillslopes. *Hydrological Processes*, *29*, 4562–4578. https://doi.org/10.1002/hyp.10468

Ghangrekar, M. M., & Chatterjee, P. (2018). Water pollutants classification and its effects on environment. In R. Das (Ed.), *Carbon nanotubes for clean water, carbon nanostructures* (pp. 11–26). Springer International Publishing. https://doi.org/10.1007/978-3-319-95603-9_2

Grimm, N. B., Faeth, S. H., Golubiewski, N. E., Redman, C. L., Wu, J., Bai, X., & Briggs, J. M. (2008). Global change and the ecology of cities. *Science*, *319*, 756–760. https://doi.org/10.1126/science.1150195

Guo, L., Chen, J., & Lin, H. (2014). Subsurface lateral preferential flow network revealed by time-lapse ground-penetrating radar in a hillslope. *Water Resources Research*, *50*, 9127–9147. https://doi.org/10.1002/2013WR014603

Hatt, B. E., Fletcher, T. D., & Deletic, A. (2009). Hydrologic and pollutant removal performance of stormwater biofiltration systems at the field scale. *Journal of Hydrology*, *365*, 310–321. https://doi.org/10.1016/j.jhydrol.2008.12.001

Haverkamp, R., Ross, P. J., Smettem, K. R. J., & Parlange, J. Y. (1994). Three-dimensional analysis of infiltration from the disc infiltrometer: 2. Physically based infiltration equation. *Water Resources Research*, *30*, 2931–2935. https://doi.org/10.1029/94WR01788

Kodešová, R., Němeček, K., Kodeš, V., & Žigová, A. (2012). Using dye tracer for visualization of preferential flow at macro- and microscales. *Vadose Zone Journal*, *11*. https://doi.org/10.2136/vzj2011.0088

Köhne, J. M., Köhne, S., & Šimůnek, J. (2009). A review of model applications for structured soils: a) Water flow and tracer transport.

Journal of Contaminant Hydrology, Preferential Flow, *104*, 4–35. https://doi.org/10.1016/j.jconhyd.2008.10.002

Lai, J., & Ren, L. (2007). Assessing the size dependency of measured hydraulic conductivity using double-ring infiltrometers and numerical simulation. *Soil Science Society of America Journal*, *71*, 1667–1675. https://doi.org/10.2136/sssaj2006.0227

Lassabatère, L., Angulo-Jaramillo, R., Soria Ugalde, J. M., Cuenca, R., Braud, I., & Haverkamp, R. (2006). Beerkan estimation of soil transfer parameters through infiltration experiments—BEST. *Soil Science Society of America Journal*, *70*, 521–532. https://doi.org/10.2136/sssaj2005.0026

Lassabatere, L., Winiarski, T., & Galvez-Cloutier, R. (2004). Retention of three heavy metals (Zn, Pb, and Cd) in a calcareous soil controlled by the modification of flow with geotextiles. *Environmental Science & Technology*, *38*, 4215–4221. https://doi.org/10.1021/es035029s

Lassabatere, L., Yilmaz, D., Peyrard, X., Peyneau, P. E., Lenoir, T., Šimůnek, J., & Angulo-Jaramillo, R. (2014). New analytical model for cumulative infiltration into dual-permeability soils. *Vadose Zone Journal*, *13*, 1–15. https://doi.org/10.2136/vzj2013.10.0181

Li, L., Jiang, L.-L., Zeng, Y., & Liu, G. (2013). Toxicity of superparamagnetic iron oxide nanoparticles: Research strategies and implications for nanomedicine. *Chinese Physics B*, *22*, Article 127503. https://doi.org/10.1088/1674-1056/22/12/127503

Louis, P., Delgado-Gonzalez, L., Lassabatère, L., Czarnes, S., Aubert, J., Imig, A., & Clément, R. (2024). Woodchip-filled trenches: A solution to enhance urban water infiltration capacity? *Geoderma*, *451*, Article 117057. https://doi.org/10.1016/j.geoderma.2024.117057

Mori, Y., & Hirai, Y. (2014). Effective Vertical Solute Transport in Soils by Artificial Macropore System. *Journal of Hazardous, Toxic, and Radioactive Waste*, *18*, Article 04014003. https://doi.org/10.1061/(ASCE)HZ.2153-5515.0000192

Mualem, Y. (1976). A new model for predicting the hydraulic conductivity of unsaturated porous media. *Water Resources Research*, *12*, 513–522. https://doi.org/10.1029/WR012i003p00513

Müller, A., Österlund, H., Marsalek, J., & Viklander, M. (2020). The pollution conveyed by urban runoff: A review of sources. *Science of the Total Environment*, *709*, Article 136125. https://doi.org/10.1016/j.scitotenv.2019.136125

Núñez-Delgado, A. (2024). Research on environmental aspects of retention/release of pollutants in soils and sorbents. What should be next? *Environmental Research*, *251*, Article 118593. https://doi.org/10.1016/j.envres.2024.118593

Pinasseau, L., Wiest, L., Volatier, L., Mermillod-Blondin, F., & Vulliet, E. (2020). Emerging polar pollutants in groundwater: Potential impact of urban stormwater infiltration practices. *Environmental Pollution*, *266*, Article 115387. https://doi.org/10.1016/j.envpol.2020.115387

R Core Team. (2024). *R: A language and environment for statistical computing*. R Foundation for Statistical Computing.

Sage, J. (2018). *L'infiltration des eaux pluviales et son impact sur la ressource en eau souterraine. Note de problématique*. https://doc.cerema.fr/Default/doc/SYRACUSE/590312/l-infiltration-des-eaux-pluviales-et-son-impact-sur-la-ressource-en-eau-souterraine-note-de-problema?_lg=fr-FR

Šimůnek, J., Angulo-Jaramillo, R., Schaap, M. G., Vandervaere, J.-P., & van Genuchten, M. T. (1998). Using an inverse method to estimate the hydraulic properties of crusted soils from tension-disc infiltrometer data. *Geoderma*, *86*, 61–81. https://doi.org/10.1016/S0016-7061(98)00035-4

Šimůnek, J., & Genuchten, M. T. (2008). Modeling nonequilibrium flow and transport processes using HYDRUS. *Vadose Zone Journal*, *7*, 782–797. https://doi.org/10.2136/vzj2007.0074

Šimůnek, J., van Genuchten, M. Th., & Šejna, M. (2016). Recent developments and applications of the HYDRUS computer software packages. *Vadose Zone Journal*, *15*, 1–25. https://doi.org/10.2136/vzj2016.04.0033

Singh, G., Kaur, G., Williard, K., Schoonover, J., & Kang, J. (2018). Monitoring of water and solute transport in the vadose zone: A review. *Vadose Zone Journal*, *17*, Article 160058. https://doi.org/10.2136/vzj2016.07.0058

Smettem, K. R. J., Parlange, J. Y., Ross, P. J., & Haverkamp, R. (1994). Three-dimensional analysis of infiltration from the disc infiltrometer: 1. A capillary-based theory. *Water Resources Research*, *30*, 2925–2929. https://doi.org/10.1029/94WR01787

Stephan, S., Jackisch, C., Tronicke, J., & Allroggen, N. (2024, April 14–19). High-resolution 4D GPR data acquisition strategy to monitor fast and small-scale subsurface flow processes (No. EGU24-12500). Presented at the EGU24, Copernicus Meetings, Vienna, Austria. https://doi.org/10.5194/egusphere-egu24-12500

Tedoldi, D., Chebbo, G., Pierlot, D., Kovacs, Y., & Gromaire, M.-C. (2016). Impact of runoff infiltration on contaminant accumulation and transport in the soil/filter media of sustainable urban drainage systems: A literature review. *Science of the Total Environment*, *569–570*, 904–926. https://doi.org/10.1016/j.scitotenv.2016.04.215

Truss, S., Grasmueck, M., Vega, S., & Viggiano, D. A. (2007). Imaging rainfall drainage within the Miami oolitic limestone using high-resolution time-lapse ground-penetrating radar. *Water Resources Research*, *43*, Article W03405. https://doi.org/10.1029/2005WR004395

Utsi, E. C. (2017). *Ground penetrating radar: Theory and practice*. Butterworth-Heinemann.

van Genuchten, M. Th. (1980). A closed-form equation for predicting the hydraulic conductivity of unsaturated soils. *Soil Science Society of America Journal*, *44*, 892–898. https://doi.org/10.2136/sssaj1980.03615995004400050002x

Wang, C., Wang, R., Huo, Z., Xie, E., & Dahlke, H. E. (2020). Colloid transport through soil and other porous media under transient flow conditions—A review. *WIREs Water*, *7*, Article e1439. https://doi.org/10.1002/wat2.1439

SUPPORTING INFORMATION

Additional supporting information can be found online in the Supporting Information section at the end of this article.

How to cite this article: Fernandes, G., Di Prima, S., Lipeme Kouyi, G., Fletcher, T. D., Donze, D., James, R., Saint-Louis, S.-M., Martini, M., Nicklason, C., & Lassabatere, L. (2025). A novel method to assess the infiltration and filtration functions of urban soils. *Vadose Zone Journal*, *24*, e70050. https://doi.org/10.1002/vzj2.70050